Rare Metal Materials and Engineering
Volume 54, Issue 11, November 2025
Available online at www.rmme.ac.cn

Science Press

Cite this article as: Zhao Lun, Sun Zhichao, Wang Chang, et al. Effect of Pore Structure on Forming Quality and Performance of Mg-5Zn Magnesium Alloy Porous Bone Repair Scaffold Fabricated by SLM[J]. Rare Metal Materials and Engineering, 2025, 54(11): 2717-2728. DOI: https://doi.org/10.12442/j.issn.1002-185X.20240618.

ARTICLE

Effect of Pore Structure on Forming Quality and Performance of Mg-5Zn Magnesium Alloy Porous Bone Repair Scaffold Fabricated by SLM

Zhao Lun[1], Sun Zhichao[1], Wang Chang[1,2], Zhang Pengsheng[2], Tang Shuai[1], Zhang Baoxin[3]

[1] State Key Laboratory of Solidification Processing, School of Materials Science and Engineering, Northwestern Polytechnical University, Xi'an 710072, China; [2] Shaanxi Key Laboratory of Biomedical Metallic Materials, Northwest Institute for Nonferrous Metal Research, Xi'an 710016, China; [3] Department of Orthopedic Surgery, the Second Affiliated Hospital of Inner Mongolia Medical University, Hohhot 010050, China

Abstract: Four types of Mg-5Zn porous scaffolds with different pore geometries, including body-centered cubic (bcc), the rhombic dodecahedron (RD), gyroid (G), and primitive (P) types, were designed and fabricated using selective laser melting. Their forming quality, compression mechanical properties, and degradation behavior were investigated. Results indicate that the fabricated scaffolds exhibit good dimensional accuracy, and the surface chemical polishing treatment significantly improves the forming quality and reduces porosity error in porous scaffolds. Compared to the ones with rod structures (bcc, RD), the scaffolds with surface structures (G, P) have less powder particle adhesion. The G porous scaffold exhibits the best forming quality for the same design porosity. The predominant failure mode of scaffolds during compression is a 45° shear fracture. At a porosity of 75%, the compression property of all scaffolds meets the compressive property requirements of cancellous bone, while bcc and G structures show relatively better compression property. After immersion in Hank's solution for 168 h, the B-2-75% pore structure scaffold exhibits severe localized corrosion, with fractures in partial pillar connections. In contrast, the G-3-75% pore structure scaffold mainly undergoes uniform corrosion, maintaining structural integrity, and its corrosion rate and loss of compressive properties are less than those of the B-2-75% structure. After comparison, the G-pore structure scaffold is preferred.

Key words: magnesium alloy porous bone repair scaffold; selective laser melting; pore structure; forming quality; mechanical property; degradation performance

1 Introduction

Implanting bone repair scaffolds provides a more effective and safer method for treating large-area bone defects. Magnesium alloys possess a low modulus of elasticity and good biodegradability. They can promote bone tissue growth, making magnesium alloy porous bone repair scaffolds broadly promising in application[1–5]. Selective laser melting (SLM) is an additive manufacturing technique that melts discrete powder materials and builds them up layer by layer, which can accurately design and efficiently fabricate scaffolds with complex internal pore structures according to the shape of the patient's bone defects to promote cell adhesion, nutrient delivery, and bone tissue regeneration[6–9]. A reasonable magnesium alloy porous scaffold should have good SLM-forming quality, adequate support strength, and favorable degradation behavior to provide a viable environment for recovering and regenerating of damaged bone tissue. However, magnesium alloys are prone to vaporization and spheroidization during

Received date: November 24, 2024
Foundation item: Science and Technology Planning Project of Inner Mongolia Science and Technology Department (2022YFSH0021); Key Research and Development Program of Shaanxi Province (2024SF2-GJHX-14, 2021SF-296)
Corresponding author: Sun Zhichao, Ph. D., Professor, State Key Laboratory of Solidification Processing, School of Materials Science and Engineering, Northwestern Polytechnical University, Xi'an 710072, P. R. China, Tel: 0086-29-88460212-802, E-mail: zcsun@nwpu.edu.cn; Zhang Pengsheng, Ph. D., Professor, Northwest Institute for Nonferrous Metal Research, Xi'an 710016, P. R. China, E-mail: zhangpengsheng2015@163.com

SLM processing[10]. The forming quality, mechanical property, and degradation performance of the scaffolds are sensitive to structural attributes such as pore units and porosity[11]. Mg-5Zn without toxic elements shows a better combination of biocompatibility and mechanical strength[12–13]. In addition, Mg-5Zn alloy powder for additive manufacturing can be prepared through mature commercialization. Therefore, studying and clarifying the ideal pore structure and properties of degradable Mg-5Zn magnesium alloy scaffolds suitable for the SLM process has a vital role in promoting the development of magnesium alloy porous bone repair scaffolds.

Compared to porous structures with inconsistent structural shapes and unordered distribution, regular porous structures with repeated arrangements of the same unit, such as rod unit structures and surface unit structures, exhibit more uniform stress distribution and are less challenging to fabricate using SLM[14–16]. Current research on the porous topology design of titanium alloys has rapidly advanced[17–19]. The porous structures used in bone repair play a crucial role in mechanical properties and influence the proliferation and differentiation of cell growth[20–22]. Porosity between 60% and 90% is suitable for bone ingrowth. Although an increase in porosity can enhance bone cell integration, it will reduce mechanical properties[23]. Lietaert et al[24] designed and fabricated porous zinc alloy scaffolds with five unit structures (diamond, octet truss, 3D Kagome, etc.) with porosity of 70% by SLM and found that the 3D Kagome structure exhibits the best yield strength. Li et al[25] fabricated topologically ordered porous magnesium (WE43) scaffolds based on diamond unit cells and found that they meet bone tissue engineering requirements. Wang et al[26] designed and fabricated three structures (biomimetic, diamond, and gyroid) of porous Jiaoda BioMg (JDBM) scaffolds by SLM, and the results showed that the gyroid scaffold has the best performance. Magnesium alloy porous scaffolds gradually degrade during service, which means that their porous structure gains more considerations than inert metal scaffolds.

The forming quality and performance of bone repair porous scaffolds are critical to their application. Xiao et al[27] utilized topological optimization to achieve a microstructure with maximum stiffness under the constraint of a specific pore volume fraction. When the minimum average pore diameter is 231 μm, the 3D geometric shape and pore morphology of metal scaffolds are reproduced with high precision. Xie et al[28] produced JDBM magnesium alloy porous scaffolds using SLM, which exhibited suitable mechanical properties and excellent osteoinductivity in vitro. However, a large amount of alloyed spherical powder residue on the surface of the porous scaffolds leads to varying degrees of obstruction in the designed structural pores, resulting in a porosity of only 32.1%, significantly lower than the intended design porosity of 80%. Liu et al[8] studied the WE43 magnesium alloy porous scaffolds fabricated using SLM, and the results showed that the spatial distribution of forming errors in different unit scaffolds varies. Also, the forming quality of the scaffolds is related to the designed porous structure. By designing the porous structure, the mechanical properties of the scaffolds can be extensively adjusted to meet the mechanical performance requirements of cancellous bone.

Appropriate degradability is another critical indicator for implanted bone repair scaffolds. Jia et al[29] studied magnesium alloy scaffolds with two types of 3D interconnected porous structures. They found that the degradation products are unrelated to the pore structure. During the degradation process, the external pore structures of both scaffolds are gradually obstructed by degradation products, leading to reduced interconnectivity between external and internal pores and varying degradation rates. Li et al[30] found that the degradation products attached to the magnesium alloy porous scaffolds after degradation have minimal impact on load-bearing. Wang et al[31] demonstrated that three types of structures (biomorph, diamond, and gyroid) fabricated via SLM exhibit sufficient degradation resistance and compressive performance for WE43 magnesium alloy porous scaffolds, meeting the requirements of bone tissue engineering. However, there are significant differences in the mechanical properties and degradation behavior among the various structured porous scaffolds. The diamond unit-cell porous magnesium alloy scaffold fabricated by SLM maintains its structural integrity after degradation. However, during this process, Young's modulus is affected by changes in the internal structure of scaffolds, attributed to localized corrosion-induced stress concentration[25]. The structural unit of porous JDBM magnesium alloy scaffolds plays a critical role in influencing compressive mechanical performance, and the degradation rate is directly correlated with the structure of the porous scaffold[26] . From the above study, the structure of magnesium alloy porous scaffolds significantly influences their forming ability, mechanical properties, and degradation performance. Further research is needed to investigate the optimal pore structure, forming quality, and performance of Mg-5Zn scaffolds.

In this study, four typical structures of Mg-5Zn porous scaffolds—body-centered cubic (bcc), rhombic dodecahedron (RD), primitive (P), and gyroid (G), based on the structural characteristics of bone repair scaffolds—with varying pore sizes were designed and fabricated by SLM. Their forming ability, mechanical properties, and degradation performance were investigated, aiming to guide the design and fabrication of Mg-5Zn alloy porous scaffolds for bone repair.

2 Experiment

2.1 Scaffold design

According to the structural characteristics of bone repair scaffolds, four types of pore geometries were designed based on the rod unit and face unit structures, including bcc, RD, P, and G types. The unit cell sizes of bcc (Fig. 1a) and RD (Fig.1b) structures are 2 mm×2 mm×2 mm and 3 mm×3 mm×3 mm, respectively. The unit cell sizes of P (Fig. 1c) and G (Fig.1d) structures are 2 mm×2 mm×2 mm and 3 mm×3 mm×3 mm, respectively. Different porosities are obtained by varying the supporting diameters of rods or the wall

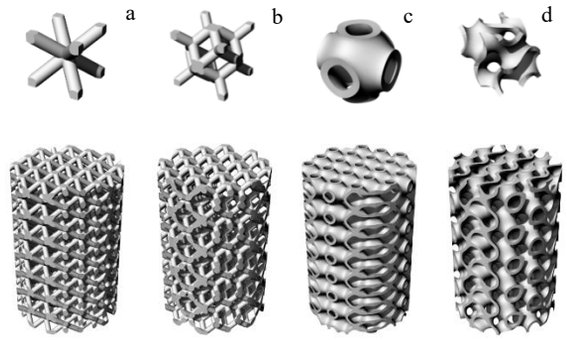

Fig.1 Unit cell structures and 3D modeling of different types of magnesium alloy porous scaffolds: (a) bcc; (b) RD; (c) P; (d) G

thicknesses of curved surfaces. Based on the manufacturing constraints of SLM equipment and the design requirements for bone repair scaffolds, each structure was designed with four different porosity models, ranging from 64% to 91%. The dimensions of the scaffolds were 10 mm×15 mm.

Additionally, for each structure, an extra-porous scaffold with porosity of 75% was designed for comparison. The pore unit dimensions were set at 2.5 mm×2.5 mm×2.5 mm. A total of 20 scaffold models were modeled, and the specific model design parameters are shown in Table 1.

The Mg-5Zn powders in this study were prepared by centrifugal atomization (Tangshan Weihao, China). The particle size distribution was mainly 20 – 80 μm, with an average particle size of 47.68 μm, as shown in Fig.2. The BLT

Table 1 Porous scaffold model parameters

Type	Sample	Rod diameter or wall thickness/mm	Porosity/%
bcc	B-2-65%	0.59	65
	B-2-69%	0.54	69
	B-2-75%	0.48	75
	B-2-79%	0.43	79
	B-2.5-75%	0.62	75
RD	R-3-70%	0.58	70
	R-3-75%	0.52	75
	R-3-80%	0.46	80
	R-3-85%	0.39	85
	R-2.5-75%	0.43	75
P	P-2-66%	0.30	66
	P-2-70%	0.26	70
	P-2-75%	0.22	75
	P-2-80%	0.18	80
	P-2.5-75%	0.27	75
G	G-3-70%	0.30	70
	G-3-75%	0.25	75
	G-3-80%	0.20	80
	G-3-85%	0.15	85
	G-2.5-75%	0.21	75

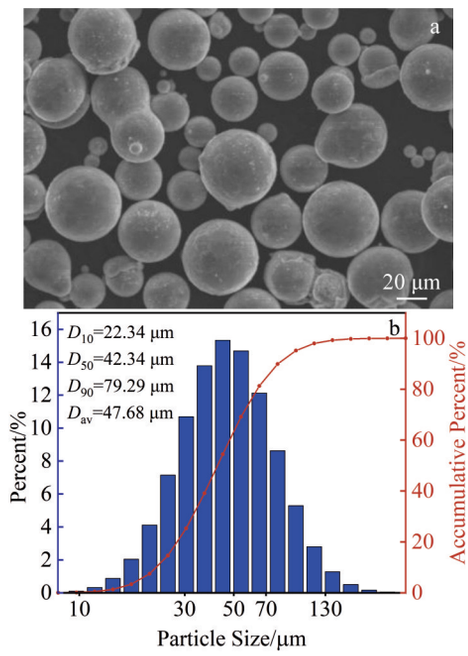

Fig.2 Morphology (a) and particle size distribution (b) of Mg-5Zn powder

S210 SLM equipment was used, equipped with a fiber laser with a maximum power of 500 W, a spot diameter of 100 μm, and a maximum forming size of 105 mm×105 mm×200 mm. Based on the previous research on SLM forming of Mg-5Zn alloy, the process parameters were selected: laser power of 70 W, scanning speed of 400 mm/s, scanning spacing of 0.06 mm, and powder layer thickness of 0.03 mm. The scanning strategy involved bidirectional scanning, with the scanning lines staggered by 67° between consecutive layers, and the forming process was performed in high-purity argon gas.

After fabrication, all the magnesium alloy porous scaffolds were ultrasonically cleaned for 4 h. The scaffolds were then chemically polished in a 5% HCl+5% HNO_3+90% C_2H_5OH solution for 120 s. The polishing process was conducted using a magnetic stirrer at 800 r/min, followed by rinsing with water and anhydrous ethanol, and the product was finally dried in a drying oven.

2.2 Experiment methods

The porosity of the prepared porous scaffold samples was measured by density balance based on the Archimedes drainage method according to the ASTMB962-08 standard, and anhydrous ethanol was used as the medium instead of water in the measurement. The macroscopic morphology, microstructures, and fracture morphology of the scaffolds were observed using the Hitachi SU5000 thermal field emission scanning electron microscope (SEM). The elemental distribution of microstructures was analyzed by the Oxford Max Ultim energy dispersive spectrometer (EDS).

The compression property of the porous magnesium alloy scaffolds was tested using a CTM8050 electronic universal testing machine. The compression speed was set at 0.9 mm/min, and the compression ratio was 50%. The

corresponding yield strength, compressive strength, elastic modulus, and failure mode were determined by analyzing the engineering stress-engineering strain curve.

The degradation behavior of porous scaffolds with a porosity of 75% in bcc structure (B-2-75%) and P structure (G-3-75%) was investigated through simulated body fluid (SBF) immersion experiments. The immersion tests followed the ASTM G31-72 standard. SBF in the immersion experiments was prepared using Hank's solution (Coolaber, China). The pH was adjusted to 7.4 at 36.5±0.5 °C. The composition of SBF is shown in Table 2.

pH measurements and the mass loss method were used to characterize the corrosion rate of porous magnesium alloy scaffolds in Hank's solution. (1) The pH of the 500 mL SBF containing the porous scaffold was measured at set intervals for pH testing. The scaffold was temporarily removed to prevent changes in pH during the test. Before testing, the pH meter should be calibrated and SBF needs to be stirred uniformly. The pH electrode should be rinsed with deionized water and dried with filter paper before each measurement. Read the pH value once the reading stabilizes. (2) For the mass loss test, the sample was immersed in a chromic acid solution (CrO_3: 200 g/L, $AgNO_3$: 10 g/L). After soaking, the sample was ultrasonically cleaned for 5 min to remove corrosion products, followed by rinsing with deionized water. The sample was thoroughly cleaned in anhydrous ethanol to remove any residual chromic acid solution from the surface and then dried before weighing. The corrosion rate of the porous scaffolds was calculated according to the ASTM G31-72 standard using the following formula:

$$\mathrm{CR} = \frac{KW}{ATD} \tag{1}$$

where CR represents the corrosion rate, mm/a; K is a constant of 8.76×10^4; W denotes the mass loss after immersion, g; A stands for the surface area of the immersed sample, cm^2; T represents the immersion time, h; D signifies the density of the immersed sample, g/cm^3.

Simultaneously, the compression property loss rates of the two types of pore structure scaffolds after immersion in Hank's solution for 168 h were statistically analyzed, and the corresponding mechanical property losses were calculated.

Table 2 Composition of Hank's SBF of 1 L

Composition	Mass/g
NaCl	8.000
KCl	0.350
Na_2HPO_4	0.400
KH_2PO_4	0.060
$MgSO_4$	0.098
$CaCl_2$	0.140
Na_2SO_4	0.072
Glucose	1.000

3 Results and Discussion

3.1 Forming quality of porous scaffolds

Fig.3 shows the surface morphologies of the four structural porous scaffolds (bcc, RD, G, and P) fabricated by SLM. Before and after chemical polishing, the fabricated magnesium alloy porous scaffolds closely match the 3D models in Fig. 1. Before chemical polishing, all porous scaffolds exhibit overall intact and uniform structures, but they suffer from significant powder adhesion and partial pore blockage. After chemical polishing, the structural morphology of the scaffolds is clearly presented, with a smooth and dense surface without apparent defects and a metallic luster. The metallographic microstructures of the four structural porous scaffolds are shown in Fig. 4, which are mainly composed of equiaxed grains and fewer columnar grains at the melt pool boundaries. The grains are uniformly refined overall, ranging from 4 μm to 13 μm in size. The primary purpose of the chemical polishing process is to remove a large amount of unmelted spherical powder from the surface of the porous scaffolds, thus reducing the roughness of the scaffold surface and improving the surface-forming quality.

To further observe the surface morphology and polishing effect of the porous scaffolds, SEM observations and analyses were conducted on the top and side surfaces of the four types of scaffolds, as shown in Fig. 5. The number of powder particles with different shapes and sizes adhered to the surface of the scaffolds before polishing is large. The depths of the particles incorporated into the support structure vary, leading to various degrees of pore blockage in the designed structure. As shown by the top morphology of the scaffolds (Fig.5a, 5e, 5i, and 5m), the adhered powder on the surface structure scaffolds is more uniform compared to the rod structure scaffolds, resulting in the overall shape of the scaffold being closer to the design. The adherent powders on the surface of the rod unit RD structure lead to severe pore blockage (Fig. 5e). From the side morphology of the scaffolds (Fig. 5c,

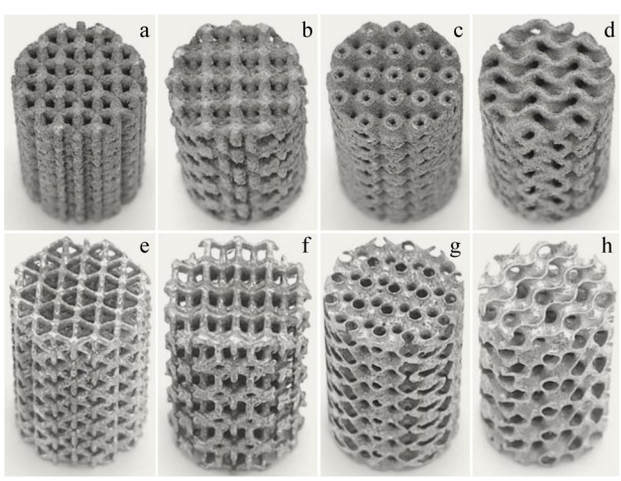

Fig.3 Photographs of different porous magnesium alloy scaffolds before (a – d) and after (e – h) chemical polishing: (a, e) bcc; (b, f) RD; (c, g) P; (d, h) G

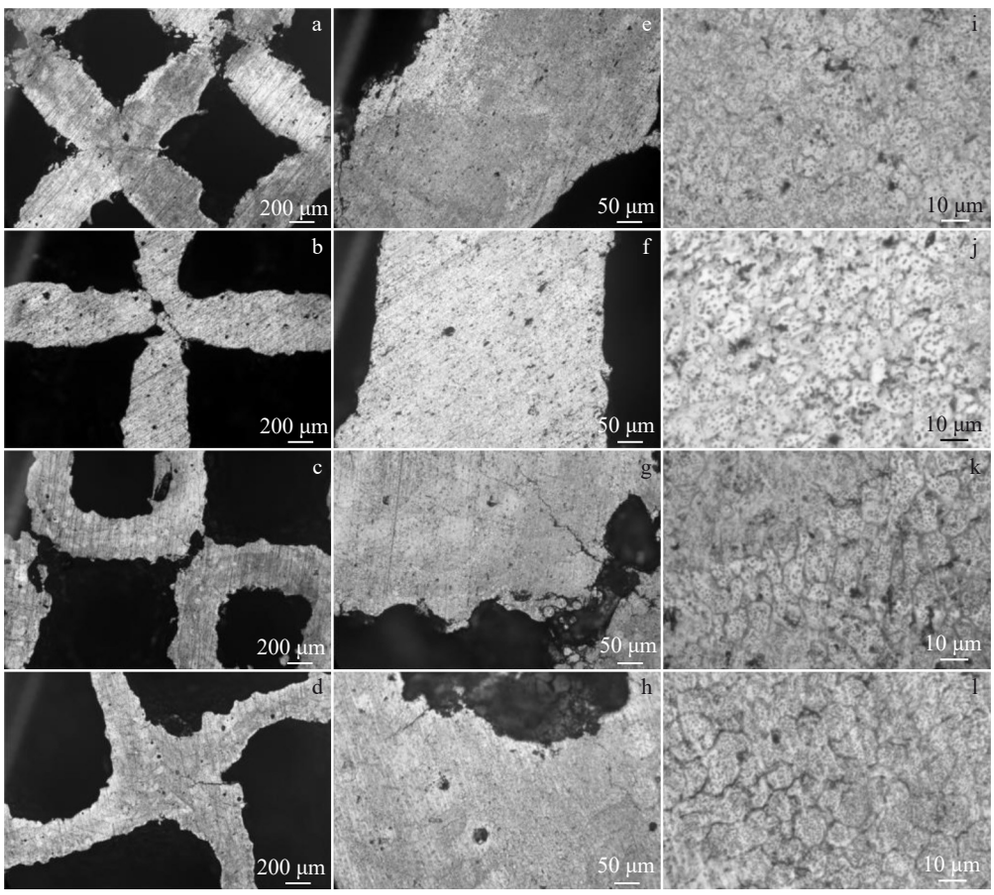

Fig.4 Metallographic microstructures of four types of scaffolds: (a, e, i) bcc; (b, f, j) RD; (c, g, k) P; (d, h, l) G

5g, 5k, and 5o), it is evident that the powder adhered to the sides of the four types of porous scaffolds is significantly larger than that on the top. Additionally, since parts of the side holes of the scaffold are suspended, the powder adhered to the surface accumulates in clumps at the unsupported and suspended areas, indicated by the red ellipses in Fig.5g.

After chemical polishing, the powders adhered to the surface of the porous scaffolds are corroded and removed, resulting in surface features that closely resemble the design models and a significant improvement in surface quality (Fig.5b, 5f, 5j, 5n, 5d, 5h, 5l, and 5p). As for the top surface, there is no significant difference between the periphery and the center of the scaffolds, and the rod diameter or wall thickness and the pore morphology are relatively good. Among them, the G structure exhibits the best quality after polishing (Fig. 5n). The connection areas of the rod unit bcc scaffold and the rod unit RD scaffold are coarser compared to the middle part of the rod, resulting in poorer uniformity of the scaffolds (Fig.5b and 5f). Similar issues also appear on the top surface. Some accumulated powder particles that are not completed corroded and removed still remain at the rod connections or suspended positions, such as in the valley area of the P structure surface (Fig. 5l). In a comprehensive comparison of surface roughness, residual powder, and uniformity, the G structure porous scaffolds are better than the other three types of porous structures.

Fig. 6 shows the porosity error data of magnesium alloy porous scaffolds obtained by comparing the measured porosity values to the design model values. As shown in Fig. 6a, it can be seen that the porosity errors of the four types of pore structure scaffolds are between 20% and 30% before chemical polishing. When the unit cell size is 3 mm, the porosity error decreases with increasing the porosity. When the porosity is 75%, the porosity error decreases with increasing the unit cell size. As the rod diameter or wall thickness increases, the porosity error decreases. After chemical polishing, the porosity errors of most porous scaffolds reduce to around 10%. For the same pore geometry scaffold, the larger the unit cell size, the smaller the error after polishing. From Fig. 5 – Fig. 6, it can be found that the appropriate chemical polishing process can effectively reduce the porosity error and the surface roughness of porous scaffolds to improve the porosity of the porous scaffolds. However, due to the structure, forming process, and forming characteristics of porous scaffolds, chemical polishing cannot eliminate the forming error of the scaffolds. Of course, chemical polishing may also lead to over-polishing in some regions of porous scaffolds of different structures, which may, on the contrary, make the porous scaffolds susceptible to stress concentration in the over-polished

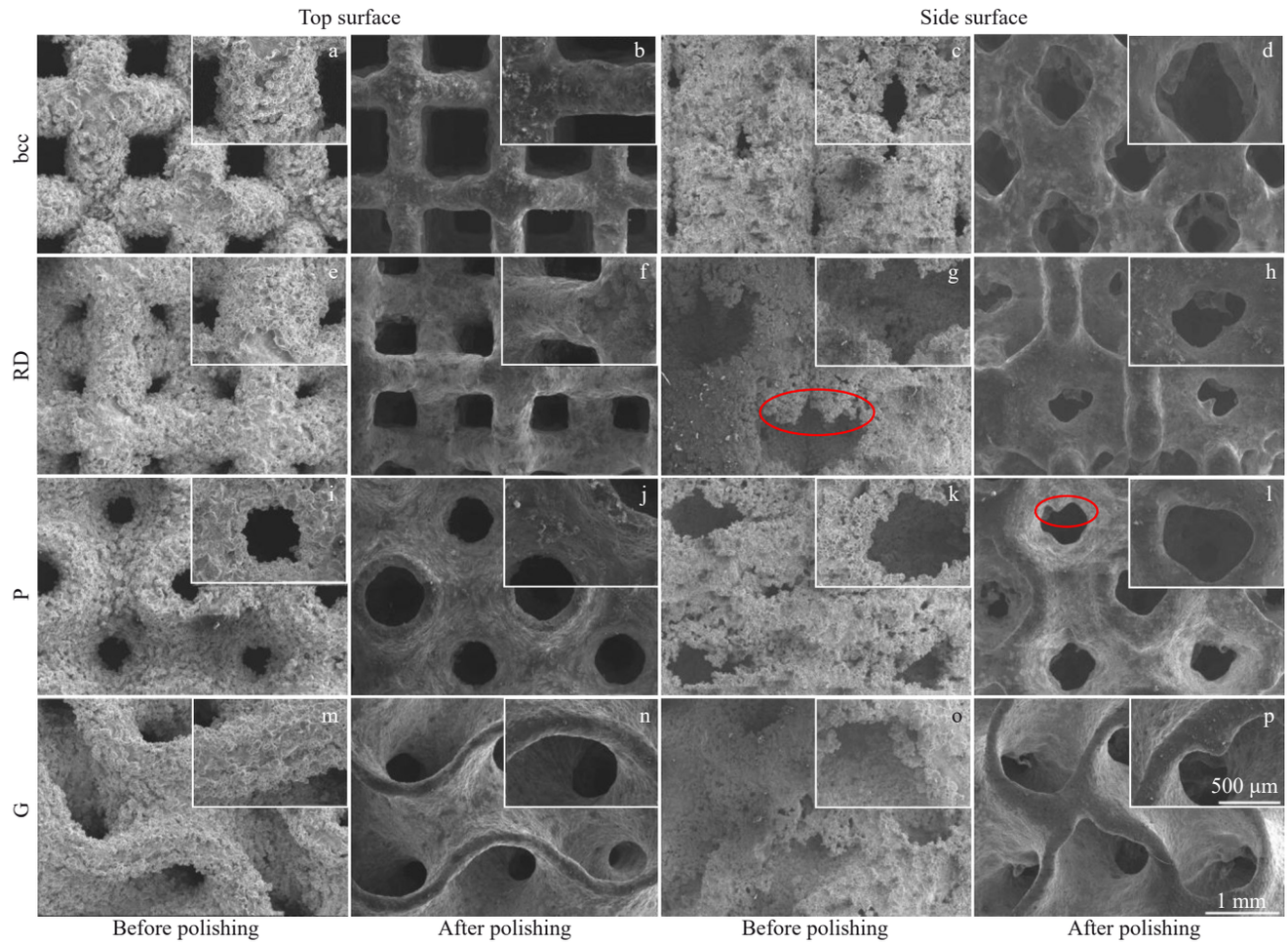

Fig.5 SEM images of top surface and side surface of different porous scaffolds before and after polishing

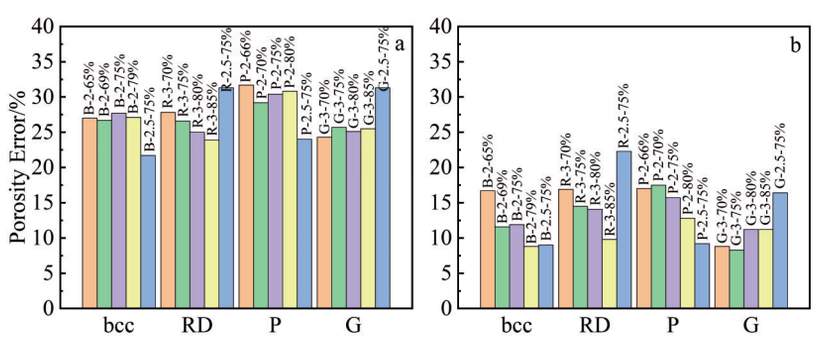

Fig.6 Porosity error of different magnesium alloy porous scaffolds before (a) and after (b) chemical polishing

regions when subjected to force or increase the degradation rate of the regions, leading to premature failure of the porous structure.

The above analysis indicates that for magnesium alloy porous scaffolds fabricated by SLM, there is a significant amount of spheroidized powder residue on the surface and the structural pores with varying degrees of blockage. This can be effectively improved by post-processing through chemical polishing. However, some powder residue remains at the rod connections or suspended positions. Chemical polishing can enhance the surface quality of the scaffolds and improve the porosity of porous scaffolds. However, it does not fundamentally eliminate forming errors. Excessive chemical polishing also negatively affects the scaffolds ' mechanical properties and degradation behavior. The pore structure is a crucial factor affecting the forming quality of the scaffolds. Regardless of polishing, the degree of powder adhesion and the forming error of surface-structure scaffolds are lower than those of rod-structure scaffolds. For bcc and RD structures, as the porosity increases, the size of the rods decreases, leading to difficulties in forming. After chemical polishing, the surface roughness, powder residue, and uniformity of G structure

porous scaffolds are superior to those of other three structures. Under the same porosity conditions, the forming quality of G structure scaffolds is the best.

3.2 Mechanical properties of porous scaffolds

The mechanical properties and compressive failure modes of four porous scaffolds with different porosities after polishing treatment were investigated by quasi-static compression experiments. Fig. 7 shows the compressive stress-compressive strain curves of the porous scaffolds, which present the typical compressive deformation characteristics of porous structures, where the stresses rapidly rise to a higher point, followed by oscillations with deformation.

The compressive stress-compressive strain curves of the four structures show weak fluctuations in the inelastic phase before reaching the compressive strength, which may be caused by the localized minor fragmentation of the porous structure before reaching the maximum stress. There are differences in the compressive stress-compressive strain curves of different porous structures, and the rod unit structure stress exhibits violent vibration with strain when the structural damage occurs (Fig. 7a – 7b). In contrast, the surface unit structure shows a more moderate magnitude of stress variation with strain (Fig. 7c – 7d). The bcc structure with rod units and the G structure with face units have higher compressive strength. For the same type of porous structure, the compressive stress-compressive strain curves are shifted downward with increasing the porosity, indicating that as porosity increases, the yield strength, compressive strength, and elastic modulus of the porous structure decrease. When the porosity of scaffolds with the same type of structural model is 75%, the initial peak stresses on the compression curve decrease with increasing the unit cell size. However, as the unit cell size decreases, the challenge of acid-etching the scaffold intensifies, resulting in more significant porosity errors, which can also impact mechanical properties.

Based on the compression curves of scaffolds designed with a porosity of 75%, the compressive strengths and elastic moduli are obtained. For B-2-75% (actual porosity=65.5%), R-3-75% (actual porosity=60.5%), P-2-75% (actual porosity=59.3%), and G-3-75% (actual porosity=66.7%) samples, the compressive strengths are 63.5, 27.5, 28.5, and 40.0 MPa, while the elastic moduli are 1231±10, 807±2, 1212±9, and 1358±5 MPa, respectively. G and bcc structures exhibit superior compression properties compared to P and RD structures, and the G structure demonstrates stronger resistance to elastic deformation.

Fig. 8 shows the failure modes of the porous scaffolds at a compression strain of 50%, exhibiting three failure modes: 45° shear failure, fragmentation, and interlayer collapse. The predominant failure mode is the 45° shear failure, closely related to the porous structure. The bcc and RD structures primarily experience 45° shear fracture (Fig. 8a – 8b) with localized fragmentation, particularly evident in the RD structure. The primary failure mode of the P structure varies with porosity. At a porosity of 49.0%, 45° shear failure occurs (Fig. 8c); at a porosity of 52.5%, both 45° shear failure and interlayer collapse are observed (Fig. 8d); when the porosity exceeds 59.3%, the sample is flattened, resulting in interlayer collapse (Fig. 8e). The G structure exhibits typical 45° shear failure. However, the shear band bends, possibly due to stress concentration at certain angles during loading.

During the compression of various porous structures, the curves show different stages, including linear-stress-increase stage, nonlinear-stress-increase stage, oscillation, and densification[25]. Before reaching the first peak, the stress exhibits slight fluctuations, indicating local fragmentation

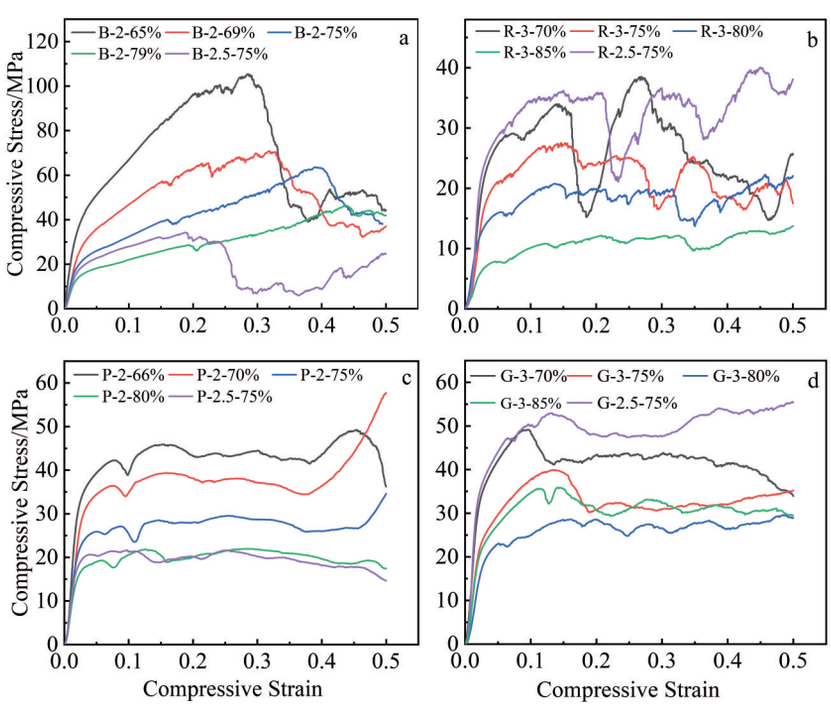

Fig.7 Compressive stress-compressive strain curves of different magnesium alloy porous scaffolds: (a) bcc; (b) RD; (c) P; (d) G

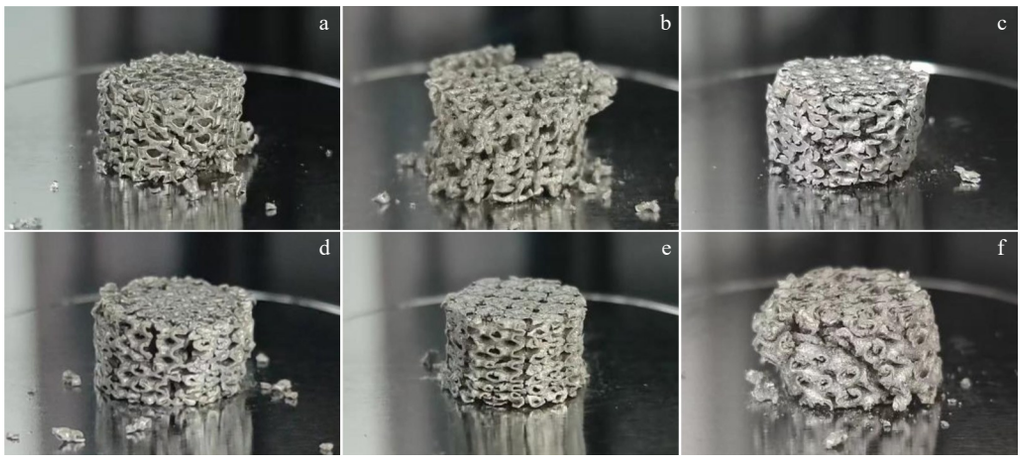

Fig.8 Compression failure mode of different porous scaffolds: (a) bcc; (b) RD; (c) P structure with a porosity of 49.0%; (d) P structure with a porosity of 52.5%; (e) P structure with a porosity of 59.3%; (f) G structure

within the porous structure, which could be related to local defects in the scaffold. The compressive properties of the four structures of porous scaffolds discussed in this study meet the requirements for cancellous bone, whose compressive strength and Young's modulus range from 0.2 MPa to 80 MPa and 0.01 GPa to 2 GPa, respectively[26,32]. At the same designed porosity (75%), the bcc porous structure and G porous structure exhibit better compressive mechanical properties, while increasing porosity leads to reduced compression property for the same structure. 45° shear fractures predominantly characterize the compression failure modes of bcc, RD, and G structures. In contrast, the failure mode of the P structure varies with porosity.

3.3 Degradation properties of porous scaffolds

Bone repair scaffolds with porosity in the range of 70%–80% exhibit good osteogenic properties, so bcc (B-2-75%) and G (G-3-75%) structure porous scaffolds with a porosity of 75% are selected for the analysis of degradation properties. Fig. 9 shows the results of the pH change curves, mass loss rates, corrosion rates, compressive stress-compressive strain curves, and mechanical properties loss of the porous scaffolds after immersion in Hank's solution for different time. Initially, the pH of Hank's solution rises rapidly, stabilizing after 12 h, with the B-2-75% structure showing a slightly higher pH than the G-3-75% samples structure during the immersion period (Fig.9a). After immersion for 168 h, the mass loss rates for B-

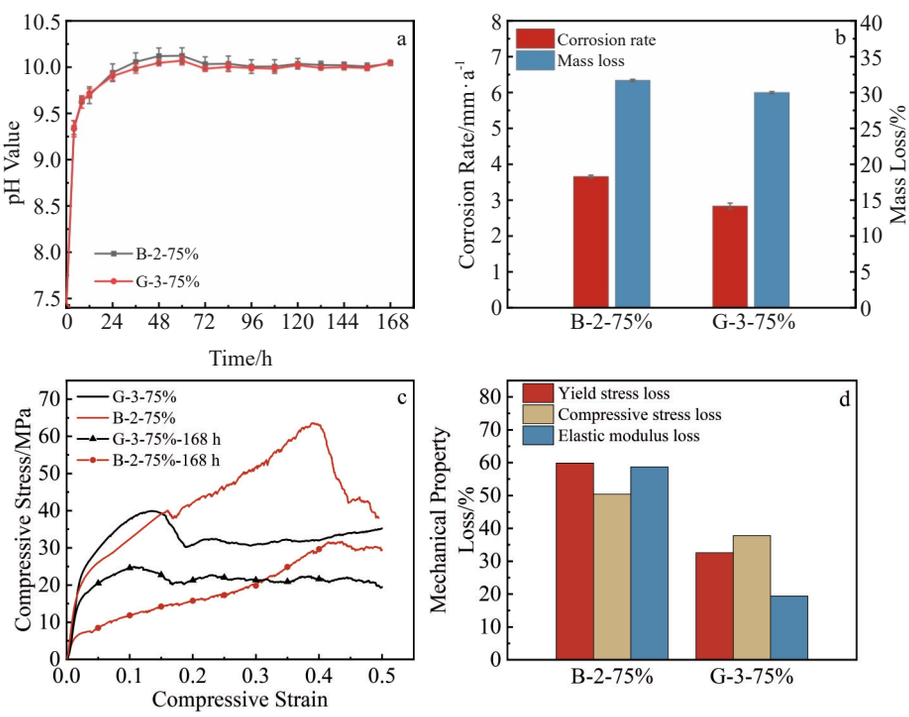

Fig.9 pH change curves of scaffolds during immersion in Hank's solution (a); mass loss and calculated corrosion rate (b), compressive stress-compressive strain curves (c), and mechanical property loss (d) of scaffolds after immersion in Hank's solution for 168 h

2-75% and G-3-75% samples are 31.7% and 30.0%, with corrosion rates of 3.66 and 2.83 mm/a, respectively (Fig. 9b). The mass loss and corrosion rate calculations for both structures are consistent with the trend in pH change, with the G-3-75% scaffold having a slightly lower corrosion rate than the B-2-75% structure, which is related to the quality of scaffold formation and structural characteristics.

After immersion, the compressive stress-compressive strain curves and mechanical property loss of the two types of scaffolds are shown in Fig. 9c and 9d, respectively. The compressive stress-compressive strain curves of the scaffolds overall decrease. For the B-2-75% scaffold, the post-immersion yield strength is 5.9 MPa, the compressive strength is 31.5 MPa, and the elastic modulus is 508±5 MPa. In contrast, the G-3-75% scaffold has a yield strength of 14.5 MPa, a compressive strength of 24.9 MPa, and an elastic modulus of 1095±5 MPa. The B-2-75% scaffold exhibits a more significant compressive property loss than the G-3-75% scaffold. The loss rates of yield strength, compressive strength, and elastic modulus for the B-2-75% scaffold exceed 50%, indicating a significant deterioration in compressive properties.

Fig. 10 shows the degradation behavior of B-2-75% and G-3-75% scaffolds. From the macroscopic morphologies of the two scaffolds before and after immersion, as demonstrated in Fig. 10a – 10c, it can be observed that the scaffolds are darkened. The surfaces are covered with corrosion products after 168 h of immersion. The white corrosion products partially block the pore structure of the scaffolds. Although the overall structure and volume do not change significantly, localized damage occurs (Fig. 10b). After removing the degradation products from the surface of the scaffolds, it is found that the pore structure of the B-2-75% scaffold becomes inhomogeneous and less intact due to localized fractures or even detachment of the rod structure. In contrast, the face unit of the G-3-75% scaffold remains relatively intact, with a visible pore structure. Only the peripheral ends of the structure suffer varying degrees of corrosion damage (Fig.10c).

Fig. 10d – 10g display the microstructural morphologies of the corrosion products after 168 h of immersion in Hank's solution. Both types of scaffold structures and their pores are covered to varying extents with corrosion products. Compared to the G-3-75% structure (Fig. 10f), the B-2-75% structure shows a more significant accumulation of corrosion products around the pores (Fig. 10d). Upon closer inspection, it is evident that the corrosion products loosely cover the scaffold surface, especially near the pore structures. Large chunks of corrosion products are present between gaps and cracks and at the scaffold surface (Fig. 10e and 10g), indicating a poor integration of the corrosion products with the scaffold matrix.

Fig. 10h – 10k show the microstructural appearances after removing corrosion products. The B-2-75% structure exhibits fractures at some rod unit junctions, with severe localized corrosion (Fig. 10h – 10i, highlighted by red ellipses). In contrast, the G-3-75% structure experiences relatively uniform corrosion, maintaining good integrity of face unit structure without being penetrated or fractured (Fig. 10j – 10k). Both structures display uniformly distributed micro-pitting on their surfaces, demonstrating the characteristic features of pitting corrosion. This is due to micro-galvanic corrosion occurring between the α-Mg matrix and the secondary phase present in the materials.

The microstructural surface morphology and corrosion products of the G-3-75% structure after Hank's immersion for 168 h are analyzed, as shown in Fig. 11, which reveals that the degradation products mainly consist of two layers. The inner layer is in contact with the substrate, whose surface exhibits numerous cracks and forms fragmented plates. In contrast, the outer layer adheres to the surface of the inner layer, predominantly containing white, clustered, and spherical particles. EDS element mappings of the corrosion products on the scaffold surface reveal the presence of O, Mg, P, Ca, Cl, and Zn as the main elements. The elements Mg and Zn are inferred to originate from the Mg-5Zn magnesium alloy substrate of the scaffold, while the elements O, P, Ca, and Cl are inferred to originate from Hank's solution. EDS results of points 1–3 of the degradation products indicate that the atomic ratio of Mg to O in the inner layer at point 1 is approximately 2:1, with less content of elements Ca and P, as shown in Table 3. The main component of the inner corrosion layer is $Mg(OH)_2$,

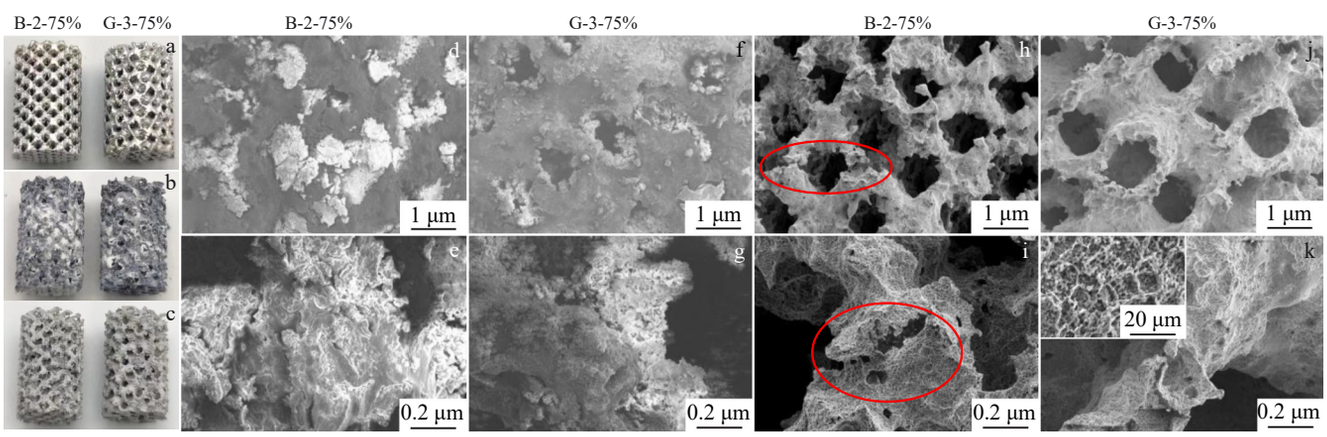

Fig.10 Macroscopic (a–c) and microscopic (d–k) morphologies of scaffolds before immersion (a), after immersion for 168 h (b, d–g), and after removal of corrosion products (c, h–k)

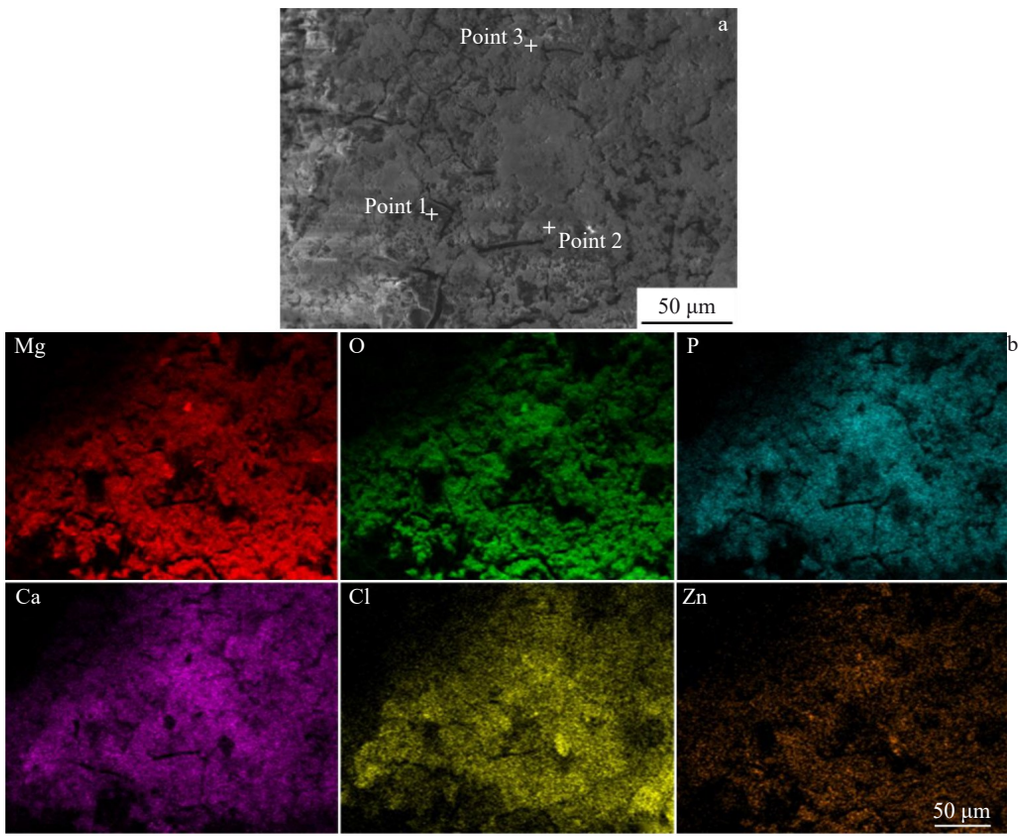

Fig.11 Microstructural surface morphology (a) and corresponding EDS element mappings (b) of G-3-75% structure after Hank's immersion for 168 h

Table 3 EDS results of points marked in Fig.11a (at%)

Element	Point 1	Point 2	Point 3
O	66.72	66.74	52.80
Mg	24.30	20.79	14.57
P	4.25	4.25	13.63
Ca	3.68	3.06	16.39
Cl	0.87	4.51	2.25
Zn	0.18	0.64	0.37

which is relatively dense and can serve as a protective barrier for further corrosion. In the outer layer (at point 2), there is a higher ratio of O to Mg atoms, suggesting that the main component is also $Mg(OH)_2$, with a significant amount of element Cl, indicating that the corrosion product $Mg(OH)_2$ is reacting with Cl^-. At point 3, in addition to O, the contents of Ca and P are higher. In comparison, the content of Mg is significantly lower compared to that in other regions, suggesting that the composition is mainly composed of calcium phosphate.

The above results indicate that, when the sample is immersed in Hank's solution, the macroscopic degradation behavior of bcc and G structure scaffolds with the same porosity is different. However, on a microscopic level, they exhibit predominantly uniform corrosion, resulting in uniform corrosion pits. The B-2-75% structure scaffold exhibits higher pH values, mass loss rates, and corrosion rates than the G-3-75% structure scaffold. The B-2-75% structure also experiences a loss rate exceeding 50% in yield strength, compressive strength, and elastic modulus, indicating more severe mechanical property degradation. This is primarily attributed to differences in degradation rates caused by scaffold structure and surface area[26,31]. Although the degradation products are unrelated to the porous structure, the external pore structure of both scaffolds gradually becomes obstructed by degradation products, leading to decreased interconnectivity between external and internal pore structures and varying degradation rates[29]. The B-2-75% structure exhibits more corrosion products on its surface and around pores, with severe localized corrosion occurring at some pillar connections, which can lead to pillar fracture or detachment, resulting in significant compression property loss. In contrast, the smoother geometric transitions of the G-3-75% structure lead to relatively uniform corrosion, better integrity of the wall structure, and no corrosion penetration or fracture, resulting in relatively minor compression property loss. The pore structure directly affects the degradation behavior of porous scaffolds and indirectly influences degradation through its impact on forming quality.

4 Conclusions

1) The Mg-5Zn porous scaffolds fabricated by SLM exhibit

overall integrity and uniformity. However, severe powder adhesion is observed on the surface with partial pore blockage. After chemical polishing, the structural morphology of the porous scaffolds is clearly presented. The surface structure (G, P) scaffolds have less powder adhesion and more minor forming errors than the rod structure (bcc, RD) scaffolds. Among scaffolds with the same design porosity, the G scaffolds show the best forming quality.

2) The four types of porous structure scaffolds show typical compressive deformation characteristics of porous structures, and they all meet the performance requirements of cancellous bone. The failure mode of the scaffolds in compression is dominated by 45° shear fracture. The failure mode of P structure scaffolds shifts from 45° shear fracture to interlayer collapse as the porosity increases from 49.0% to 52.5%. The bcc and G structure have better compressive mechanical properties with the same design porosity, and the compressive properties decrease with increasing the scaffold porosity in the same structure.

3) After immersion in Hank ' s solution for 168 h, the scaffolds exhibit primarily pitting corrosion, resulting in uniform corrosion pits. The G-3-75% structure scaffolds have relatively more uniform corrosion, slower degradation, better wall structural integrity, and less loss of compressive property due to smoother geometric transitions. In contrast, the B-2-75% structural scaffold experiences severe local corrosion and partial pillar fracture, significantly losing compression mechanical properties.

4) The G structure has excellent structural characteristics, resulting in the best overall performance in forming quality, compressive mechanical properties, and degradation behavior. Therefore, the G pore structure scaffold is preferred.

References

1 DebRoy T, Wei H L, Zuback J S *et al*. *Progress in Materials Science*[J], 2018, 92: 112

2 Ng C C, Savalani M M, Man H C *et al*. *Virtual and Physical Prototyping*[J], 2010, 5(1): 13

3 Shuai Cijun, Yang Youwen, Wu Ping *et al*. *Journal of Alloys and Compounds*[J], 2017, 691: 961

4 Wei Kaiwen, Gao Ming, Wang Zemin *et al*. *Materials Science and Engineering A*[J], 2014, 611: 212

5 Esmaily M, Zeng Z, Mortazavi A N *et al*. *Additive Manufacturing*[J], 2020, 35: 101321

6 Wysocki B, Idaszek J, Szlązak K *et al*. *Materials*[J], 2016, 9(3): 197

7 Bozkurt Yahya, Karayel Elif. *Journal of Materials Research and Technology*[J], 2021, 14: 1430

8 Liu Jinge, Liu Bingchuan, Min Shuyuan *et al*. *Bioactive Materials*[J], 2022, 16: 301

9 Qin Yu, Wen Peng, Voshage Maximilian *et al*. *Materials & Design*[J], 2019, 181: 107937

10 Liu Shuai, Guo Hanjie. *Materials*[J], 2020, 13(16): 3632

11 Zhang M, Lin R, Wang X *et al*. *Science Advance*[J], 2020, 6(12): eaaz6725

12 Jiang Pingli, Blawert Carsten, Zheludkevich Mikhail L *et al*. *Corrosion and Materials Degradation*[J], 2020, 1: 92

13 Asadollahi Mohammad, Gerashi Ehsan, Alizadeh Reza *et al*. *Journal of Materials Research and Technology*[J], 2022, 21: 4473

14 Cai Shuhua, Lei Ting, Li Nianfeng *et al*. *Materials Science and Engineering C*[J], 2012, 32(8): 2570

15 Zadpoor A A. *Journal of Materials Chemistry B*[J], 2019, 7(26): 4088

16 Zhang Jianguo, Wang Guan, Chen Peng *et al*. *Rare Metal Materials and Engineering*[J], 2023, 52(12): 4029

17 Pesode Pralhad, Barve Shivprakash. *Bioprinting*[J], 2023, 36: e00318

18 Song Changhui, Liu Lisha, Deng Zhenghua *et al*. *Journal of Materials Research and Technology*[J], 2023, 23: 2626

19 Fan Yongxia, Lin Yan, Ao Qingbo *et al*. *Rare Metal Materials and Engineering*[J], 2023, 52(10): 3630 (in Chinese)

20 Guo Liyao, Ataollah Naghavi Seyed, Wang Ziqiang *et al*. *Materials & Design*[J], 2022, 216: 110552

21 Van Bael S, Chai Y C, Truscello S *et al*. *Acta Biomaterialia*[J], 2012, 8(7): 2824

22 Deng F, Liu L, Li Z *et al*. *Journal of Biological Engineering*[J], 2021, 15(1): 4

23 Bobbert F S L, Lietaert K, Eftekhari A A *et al*. *Acta Biomaterialia*[J], 2017, 53: 572

24 Lietaert K, Zadpoor A A, Sonnaert M *et al*. *Acta Biomaterialia* [J], 2020, 110: 289

25 Li Y, Zhou J, Pavanram P *et al*. *Acta Biomaterialia*[J], 2018, 67: 378

26 Wang Yinchuan, Fu Penghuai, Wang Nanqing *et al*. *Engineering*[J], 2020, 6(11): 1267

27 Xiao Dongming, Yang Yongqiang, Su Xubin *et al*. *Transactions of Nonferrous Metals Society of China*[J], 2012, 22(10): 2554

28 Xie K, Wang N, Guo Y *et al*. *Bioactive Materials*[J], 2022, 8: 140

29 Jia Gaozhi, Chen Chenxin, Zhang Jian *et al*. *Corrosion Science*[J], 2018, 144: 301

30 Li Y, Jahr H, Pavanram P *et al*. *Acta Biomaterialia*[J], 2020, 101: 646

31 Wang Chaoxin, Min Shuyuan, Liu Jinge *et al*. *Journal of Magnesium and Alloys*[J], 2023, 12(11): 4509

32 Yusop A H, Bakir A A, Shaharom N A *et al*. *International Journal of Biomaterials*[J], 2012(1): 641430

不同构型Mg-5Zn镁合金多孔骨修复支架SLM成形质量与性能

赵　伦[1]，孙志超[1]，王　昌[1,2]，张鹏省[2]，汤　帅[1]，张葆鑫[3]

(1. 西北工业大学 材料学院 凝固技术全国重点实验室，陕西 西安 710072)

(2. 西北有色金属研究院 陕西省医用金属材料重点实验室，陕西 西安 710016)

(3. 内蒙古医科大学第二附属医院 骨科，内蒙古 呼和浩特 010050)

摘　要：设计并通过激光选区熔化技术制备了体心立方型（bcc）、菱形十二面体（RD）、螺旋型（G）和简单立方型（P）四种Mg-5Zn多孔支架，研究了其成形质量、压缩力学性能和降解行为。结果表明，所制备的支架具有较好的还原度，表面化学抛光处理显著改善了支架成形质量，并降低多孔支架的孔隙误差。面结构（G，P）支架粘附粉末的程度较杆结构（bcc，RD）轻，成形误差较小。相同设计孔隙率下，G构型支架的成形质量最佳。压缩时支架的失效模式以45°剪切断裂为主。孔隙率为75%时，四种构型支架的压缩性能都满足松质骨的压缩性能要求，bcc和G构型支架压缩性能相对较好。Hank's溶液浸泡168 h后，B-2-75%构型支架局部腐蚀较为严重，部分支柱连接处发生断裂；G-3-75%构型支架以均匀腐蚀为主，结构保持较为完整，腐蚀速率和压缩性能损失小于B-2-75%结构。经综合对比，优选G构型。

关键词：镁合金多孔骨修复支架；激光选区熔化；孔隙结构；成形质量；力学性能；降解性能

作者简介：赵　伦，男，1998年生，硕士生，西北工业大学材料学院凝固技术全国重点实验室，陕西 西安 710072，E-mail：zhaolun0009@163.com